Journal of Medical Imaging

MedicalImaging.SPIEDigitalLibrary.org

Connecting Markov random fields and active contour models: application to gland segmentation and classification

Jun Xu
James P. Monaco
Rachel Sparks
Anant Madabhushi

SPIE.

Jun Xu, James P. Monaco, Rachel Sparks, Anant Madabhushi, "Connecting Markov random fields and active contour models: application to gland segmentation and classification," *J. Med. Imag.* **4**(2), 021107 (2017), doi: 10.1117/1.JMI.4.2.021107.

Connecting Markov random fields and active contour models: application to gland segmentation and classification

Jun Xu,[a,*,†] James P. Monaco,[b,†] Rachel Sparks,[c] and Anant Madabhushi[d]
[a]Nanjing University of Information Science and Technology, Jiangsu Key Laboratory of Big Data Analysis Technique, Nanjing, China
[b]Inspirata, Tampa, Florida, United States
[c]University College of London, Center for Medical Image Computing, London, United Kingdom
[d]Case Western Reserve University, Department of Biomedical Engineering, Cleveland, Ohio, United States

Abstract. We introduce a Markov random field (MRF)-driven region-based active contour model (MaRACel) for histological image segmentation. This Bayesian segmentation method combines a region-based active contour (RAC) with an MRF. State-of-the-art RAC models assume that every spatial location in the image is statistically independent, thereby ignoring valuable contextual information among spatial locations. To address this shortcoming, we incorporate an MRF prior into energy term of the RAC. This requires a formulation of the Markov prior consistent with the continuous variational framework characteristic of active contours; consequently, we introduce a continuous analog to the discrete Potts model. Based on the automated segmentation boundary of glands by MaRACel model, explicit shape descriptors are then employed to distinguish prostate glands belonging to Gleason patterns 3 (G3) and 4 (G4). To demonstrate the effectiveness of MaRACel, we compare its performance to the popular models proposed by Chan and Vese (CV) and Rousson and Deriche (RD) with respect to the following tasks: (1) the segmentation of prostatic acini (glands) and (2) the differentiation of G3 and G4 glands. On almost 600 prostate biopsy needle images, MaRACel was shown to have higher average dice coefficients, overlap ratios, sensitivities, specificities, and positive predictive values both in terms of segmentation accuracy and ability to discriminate between G3 and G4 glands compared to the CV and RD models. [DOI: 10.1117/1.JMI.4.2.021107]

Keywords: digital pathology; prostate cancer grading; gland segmentation; Markov random field.

Paper 16168SSR received Aug. 2, 2016; accepted for publication Feb. 20, 2017; published online Mar. 28, 2017.

1 Introduction

Image segmentation remains an important task in computer vision. In the 1980s, researchers introduced two important segmentation methodologies: Markov random fields (MRFs) in 1984[1] and active contours (ACs) in 1988.[2] Both methods have since been adapted to address a variety of segmentation problems. MRFs have employed adaptive clustering,[3] multiresolution analysis,[4] and complex boundary models[5] to effectively partition mammographic,[6] multimodal,[7] magnetic resonance,[8–10] and color[11] images. AC models have been used to track cell locomotion,[12] analyze cardiac images,[13–18] segment retinal vessels,[19] and interrogate histopathological sections.[20,21]

Although the two methods are ostensibly very different—MRFs utilize a discrete Bayesian approach while ACs employ a continuous, variational paradigm—they share an important unifying concept: both perform segmentation via the minimization of energy functions that map each possible segmentation to a real number indicating its quality. This naturally poses the question of whether an energy function from one method can be adapted for use with the other. Such an adaptation strategy would be significant since MRFs and ACs do not share the same strengths and weaknesses. MRFs effectively model statistical dependencies among neighboring regions, whereas ACs readily incorporate global image statistics and boundary information.

In this paper, we extend our preliminary work in Ref. 22 to introduce a method for incorporating an MRF energy function into an AC energy functional—an energy functional is the continuous equivalent of a discrete energy function. This provides a significant advantage over traditional AC formulations as the MRF energy function can account for local statistical dependencies within the data (e.g., between pixels). Since typical AC energy functionals consist of a single integral over a closed contour (e.g., $\oint f(s)\mathrm{d}s$), they cannot model dependencies between different points on the contour, except to the limited degree allowed by higher order derivatives (e.g., curvature). Incorporating dependencies requires more complex energy functionals such as modeling pairwise interactions via: $\oint\oint f(s,s')\mathrm{d}s'\mathrm{d}s$. Previous work has leveraged sophisticated functions to define higher-order AC models,[23] which employ multiple integrals to establish shape priors for circles[24] and linear networks.[25] Implementing the Mumford Shah functional,[26] the Chan and Vese (CV)[27] model implicitly accounts for dependencies by using the mean intensity for foreground and background regions (defined as the level set) to evolve the contour. Recently, in Refs. 28 and 29, an MRF term was embedded into the level set energy functional to incorporate contextual information in the level set energy functional. However the MRF term in Ref. 28 was embedded as a distinct term via a nonlinear function for calculating the differences between background and foreground intensity information

*Address all correspondence to: Jun Xu, E-mail: xujung@gmail.com

†Jun Xu and James P. Monaco are joint first authors.

2329-4302/2017/$25.00

within pixel neighborhoods. Our method involves computing the differences via a convolutional operator within pixel neighborhoods. The work in Ref. 29 was inspired by our previous work in Ref. 22 where the MRF prior was incorporated into the energy term of local region-based active contour (RAC) model.

Despite some previous notable exceptions,[26] the incorporation of spatial dependencies into ACs remains a largely unsolved problem. This becomes clear when we examine statistical AC models that derive their energy functionals from probability distributions. The first statistical ACs, proposed by CV[27] and extended by Rousson and Deriche (RD),[30] model each pixel (more precisely its continuous analog) as an independent, identically distributed (i.i.d.) Gaussian random variable. Although later works have enhanced these methods, the i.i.d. assumption persists.

Unlike ACs, MRFs model depends among random variables using a Bayesian paradigm. The goal of this paper is to convert an MRF energy function into an AC energy functional, allowing ACs to incorporate spatial context. Specifically, we consider spatially invariant MRFs that use single and pairwise interactions to classify objects into two classes (i.e., foreground and background). We will demonstrate how an MRF energy function that satisfies these conditions can be expressed as an AC functional. Unlike previous approaches that have attempted to embed the MRF term to a level set formulation, the advantage of our work is that the MRF term can be easily implemented. Moreover, the MRF operator [see Eq. (22)] has a general form that allows for construction of different kernels for incorporating spatial context.

To demonstrate the utility of incorporating spatial information into an AC model, we use an MRF-driven region-based AC model (MaRACel) to reliably segment gland lumen (cavity through which hormonal secretions are transported) in digitized hematoxylin and eosin (H&E)-stained prostate tissues. Gland lumen morphology has been shown to be associated with Gleason patterns of prostate cancer.[31] The Gleason grading system is based on the architectural and morphological patterns of the prostate glands in cancer. A gland comprises lumen area, epithelial cytoplasm, and epithelial nuclei.[32] However, gland lumen is a difficult segmentation problem due to: (1) the number, size, and shape of glands can vary considerably and (2) small holes or tears in the tissue resemble glands and present formidable confounders. In Ref. 33, graph theory techniques were employed to segment glands. In Ref. 34, structural features extracted from gland shape were used to classify a tissue pattern into three major categories: benign, grade 3 carcinoma, and grade 4 carcinoma. In Ref. 35, a reversible jump Markov chain Monte Carlo method was used to model glandular structures in both healthy and cancerous tissues. An object-graph-based approach was presented in Ref. 36 to segment glands while a level set-based model was presented in Ref. 32 for gland detection and segmentation.

In this paper, we demonstrate how the incorporation of contextual information into the AC framework can be used to improve segmentation performance by predisposing the segmentations to certain shapes without restricting their specific size and number. Our solution represents a contrasting approach to most current AC models, which either neglect shape information entirely or—if they do consider shape—require that the objects have nearly identical shapes and sizes.[24] To further validate the utility of our model, we consider the task of differentiating Gleason pattern 3 (G3) from pattern 4 (G4). In this paper, we employ MaRACel to provide automatic segmentation with the explicit shape descriptors (ESD) framework, presented in Refs. 37 and 38 to automatically grade roughly 350 prostate biopsy images using gland morphology.

The rest of this paper is organized as follows. A review of MRFs and notations is presented in Sec. 2. A detailed description on integration of MRFs and ACs is presented in Secs. 3 and 4. The description of ESD for gland classification is presented in Sec. 5. The experimental setup and comparative strategies are discussed in Sec. 6. The experiment results and discussions are reported in Sec. 7. Concluding remarks are presented in Sec. 8. The detailed derivative of the curve evolution functional for the MaRACel model is presented in the Appendix.

2 Review of Markov Random Fields

2.1 *Preliminaries*

Let the set $S = \{\{i,j\}|1 \le i \le H, 1 \le j \le W\}$ reference a rectangular lattice of $N = W \times H$ pixel locations. Each pixel $s \in S$ has two associated random variables: $X_s \in \Lambda \equiv \{\omega_1, \omega_2, \ldots, \omega_L\}$ indicating its state (class) and $Y_s \in \mathbb{R}^D$ representing its D-dimensional feature vector. Particular instances of X_s and Y_s are denoted by the lowercase variables $x_s \in \Lambda$ and $y_s \in \mathbb{R}^D$. Let $\mathbf{X} = (X_1, X_2, \ldots, X_N)$ and $\mathbf{Y} = (Y_1, Y_2, \ldots, Y_N)$ refer to all random variables X_s and Y_s in aggregate. The state spaces of $\mathbf{X}$ and $\mathbf{Y}$ are the Cartesian products $\Omega = \Lambda^N$ and $\mathbb{R}^{D\times N}$. Instances of $\mathbf{X}$ and $\mathbf{Y}$ are denoted by the lowercase variables $\mathbf{x} = (x_1, x_2, \ldots, x_N) \in \Omega$ and $\mathbf{y} = (y_1, y_2, \ldots, y_N) \in \mathbb{R}^{D\times N}$, respectively. $y(s)$ is the function that assigns intensity values to pixel s, $\phi(t,s)$ is the level set function, S_1 is the foreground region $S_1 = \{s \in S : \phi(s) > 0\}$, S_{-1} is the background region $S_{-1} = \{s \in S : \phi(s) < 0\}$, $\mathbb{C}$ is the contours or zero level set $\mathbb{C} = \{s \in S : \phi(s) = 0\}$, $S = S_1 \cup S_{-1} \cup \mathbb{C}$ is a bounded open set in $\mathbb{R}^2$, $H(\phi)$ is a Heaviside function $H(\phi) = \begin{cases} 1, & \phi(c) \ge 0; \\ 0, & \phi(c) < 0. \end{cases}$, $\delta(\phi)$ is the delta function $\delta(\phi) = \begin{cases} +\infty, & \phi(c) = 0; \\ 0, & \phi(c) \ne 0. \end{cases}$, $\mathcal{A}(\cdot)$ is the set of pixels contained within the boundary of the object, and $\|\cdot\|$ is the L_2 norm.

Let $G = \{S, E\}$ establish an undirected graph structure, where S and E are the vertices (sites) and edges, respectively. A clique c is any subset of S, which constitutes a fully connected subgraph of G. The set $\mathcal{C}$ contains all possible cliques. A neighborhood η_s is the set containing all sites that share an edge with s. If P is a probability measure defined over Ω, then the random variable $\mathbf{X}$ governed by the triplet (G, Ω, P) is called a random field. Furthermore, $\mathbf{X}$ is an MRF if its local conditional probability density functions satisfy the Markov property: $P(X_s = x_s|\mathbf{X}_{-s} = \mathbf{x}_{-s}) = P(X_s = x_s|\mathbf{X}_{-s} = \mathbf{x}_{\eta_s})$, where $\mathbf{x}_{-s} = (x_1, \ldots, x_{s-1}, x_{s+1}, \ldots, x_N)$, $\mathbf{x}_{\eta_s} = (x_{\eta_s(1)}, \ldots, x_{\eta_s(|\eta_s|)})$, and $\eta_s(i) \in S$ is the i'th element of the set η_s. Note that in places where it does not create ambiguity, we will henceforth simplify the probabilistic notations by omitting the random variables, e.g., $P(\mathbf{x}) \equiv P(\mathbf{X} = \mathbf{x})$.

The Hammersley–Clifford theorem states that a random field $\mathbf{X}$ is an MRF if, and only if, its joint probability density function can be expressed as a Gibbs distribution[39]

$$P(\mathbf{x}) = \frac{1}{Z}\exp\{-U(\mathbf{x})\}, \tag{1}$$

where $U(\mathbf{x}) = \sum_{c\in\mathcal{C}} V_c(\mathbf{x})$ is the energy function, Z is the normalizing constant, and V_c are functions, called clique potentials, that depend only on those x_s such that $s \in c$. The local conditional probability density functions (LCPDFs) are defined as follows:

$$P(x_s|\mathbf{x}_{\eta_s}) = \frac{1}{Z_s(\mathbf{x})}\exp\{-U_s(\mathbf{x})\}, \tag{2}$$

where $\mathbf{x}_{\eta_s} = \{x_r, r \in \eta_s\}$, $U_s(\mathbf{x}) = \sum_{c\in\mathcal{C}_s} V_c(\mathbf{x})$ is the local energy, $\mathcal{C}_s$ represents $\{c \in \mathcal{C}: s \in c\}$, and $Z_s(\mathbf{x})$ is the normalizing coefficient. Note that the MRF $\mathbf{X}$ is completely defined by its LCPDFs, which also happen to be Gibbs distributions. For proofs of Markov formulations and theorems, see Geman.[40]

2.2 *Assumed Conditions and Implications*

In this work, we stipulate the following (rather typical) conditions:

1. The range of X_s is $\Lambda = \{-1,1\}$, i.e., background (-1) or foreground (1).
2. All cliques c contain either one or two elements.
3. The image boundaries are toroidal, i.e., they wrap around at the edges of the images.
4. The LCPDFs are spatially invariant, implying that:
   - the neighborhoods η_s are spatially invariant
   - the clique potentials are spatially invariant.
5. The pairwise clique potentials are not biased toward either state, i.e., $V_{\{s,r\}}(\mathbf{x}) = V_{\{s,r\}}(-\mathbf{x})$.

Under these assumptions, the energy $U(\mathbf{x})$ in Eq. (1) can be simplified as follows:

$$\begin{aligned} U(\mathbf{x}) &= \sum_{s\in S} V_{\{s\}}(\mathbf{x}) + \sum_{\{s,r\}\in\mathcal{C}} V_{\{s,r\}}(\mathbf{x}) \\ &= \sum_{s\in S} \alpha x_s + \frac{1}{2}\sum_{s\in S}\sum_{r\in\eta_s} \beta_{|s-r|} x_s x_r \\ &= \frac{1}{2}\sum_{s\in S}\{x_s[2\alpha + (\beta * x)_s]\}, \end{aligned} \tag{3}$$

where $\alpha \in \mathbb{R}$, $|s-r|$ is the Euclidean distance between pixels s and r, * denotes convolution, and β is a finite impulse response filter with coefficients $\beta_{|s-r|} \in \mathbb{R}$. Note that $\beta_0 = 0$ and that if η_s is the typical four-connected neighborhood, then Eq. (3) devolves to the Ising model.[41]

2.3 *Maximum a Posteriori Estimation*

Given an observation of the feature vectors $\mathbf{Y}$, we would like to estimate the states $\mathbf{X}$. The preferred method is maximum *a posteriori* (MAP) estimation,[42] which entails maximizing the following quantity over all $\mathbf{x} \in \Omega$:

$$P(\mathbf{x}|\mathbf{y}) = \frac{P(\mathbf{y}|\mathbf{x})P(\mathbf{x})}{P(\mathbf{y})} \propto P(\mathbf{y}|\mathbf{x})P(\mathbf{x}), \tag{4}$$

where $\propto$ indicates proportionality. The first term in Eq. (4) reflects the influence of the feature vectors. It can be simplified by assuming that all Y_s are conditionally independent given their associated X_s. This assumption implies that if the class X_s of site s is known then the classes and features of the remaining sites provide no additional information when estimating Y_s. As a result we have the following:

$$P(\mathbf{y}|\mathbf{x}) = \prod_{s\in S} P(y_s|x_s). \tag{5}$$

Instead of directly maximizing Eq. (4), it is easier (and equivalent) to maximize its natural logarithm:

$$\begin{aligned} \ln P(\mathbf{x}|\mathbf{y}) &\propto \ln P(\mathbf{x}) + \ln P(\mathbf{y}|\mathbf{x}) \\ &= -U(\mathbf{x}) - \ln Z + \sum_{s\in S} \ln P(y_s|x_s) \\ &\propto \sum_{s,x_s=1}\left[\alpha + \frac{1}{2}(\beta * x)_s + \ln P(y_s|1)\right] \\ &\quad - \sum_{s,x_s=-1}\left[\alpha + \frac{1}{2}(\beta * x)_s - \ln P(y_s|-1)\right]. \end{aligned} \tag{6}$$

Since $\ln Z$ is a constant, and thus is irrelevant to maximization, we drop it from the final equation.

3 From Markov Random Fields to Active Contours

3.1 *Energy Functional*

The goal is to now demonstrate how Eq. (6) can be expressed as a continuous AC functional. First, we establish the necessary notation. To the greatest extent possible, we will reuse the symbols from Sec. 2 since their meanings remain analogous in the AC framework. Let $S \subset \mathbb{R}^2$ establish the image region. Let the function y: $S \to \mathbb{R}^D$ reflect observations over S. Let the function x: $S \to \Lambda \equiv \{-1,1\}$ map each point s to either the background or foreground; specifically, x partitions S into the regions S_1 (foreground) and S_{-1} (background) by contour $\mathbf{C}$, where $S_1 \cup S_{-1} \cup \mathbf{C} = S$. Finally, let $X(s)$ and $Y(s)$ represent the stochastic processes associated with the functions $x(s)$ and $y(s)$. Note that for the AC notation we replace the subscript s used for MRFs with the parenthesized (s); this serves to differentiate the discrete process X_s from the continuous process $X(s)$.

Given the previous definitions, we now examine MAP estimation for ACs.[30] The goal of MAP estimation is to identity the segmentation x by maximizing the following:

$$\ln P(\mathbf{x}|\mathbf{y}) \propto \ln P(\mathbf{y}|\mathbf{x}) + \ln P(\mathbf{x}). \tag{7}$$

Assuming conditional independence as before results in the following simplification:

$$P(\mathbf{y}|\mathbf{x}) = \prod_{s\in S} P(y_s|x_s)^{ds}, \tag{8}$$

where the volume ds (i.e., a pixel or volume of infinitesimal size) assures the proper continuum limit.[30]

Like x, the level set[43] function ϕ: $S \to \mathbb{R}$ also partitions S into S_1 (foreground) and S_{-1} (background): if $\phi(s) > 0$ then $s \in S_1$ belongs to the foreground and if $\phi(s) < 0$ then $s \in S_{-1}$ belongs to the background. Consequently, the functions ϕ and x are related as follows: $x(s) = 2H[\phi(s)] - 1$, where $H(\cdot)$ is the

Heaviside function. Using the discussed notation—while dropping the explicit dependence on s for succinctness—it is straight-forward to formulate Eqs. (6) or (7) as a continuous energy functional

$$\begin{aligned}E_{\mathrm{MAP}}(\phi) &= \int_{S_1}\left[\alpha+\frac{1}{2}(\beta*x)+\ln P(y|1)\right]\mathrm{d}s \\ &\quad -\int_{S_{-1}}\left[\alpha+\frac{1}{2}(\beta*x)-\ln P(y|-1)\right]\mathrm{d}s \\ &= \int_{S} H(\phi)\left[\alpha+\frac{1}{2}(\beta*x)+\ln P(y|1)\right] \\ &\quad -[1-H(\phi)]\left[\alpha+\frac{1}{2}(\beta*x)-\ln P(y|-1)\right]\mathrm{d}s \\ &= \int_{S} H(\phi)[2\alpha+(\beta*x)+\ln P(y|1)-\ln P(y|-1)] \\ &\quad -\frac{1}{2}(\beta*x)-\alpha+\ln P(y|-1)\mathrm{d}s, \end{aligned} \tag{9}$$

where * is the convolutional operation and defined as

$$(\beta*x)(s)=\int_S x(r)\beta(s-r)\mathrm{d}r \tag{10}$$

and $\beta(s)$ is a continuous filter with $\beta(0)=0$. Note that if $\alpha\equiv\beta\equiv 0$ and all $P[y(s)|x(s)]$ are identical Gaussian densities, then Eq. (9) reduces to the region term introduced by Zhu and Yuille[44] and later extended by RD.[30] In summary, Eq. (9) is the AC formulation of the MRF energy function given in Eq. (6).

3.2 *Evolution Equation*

The curve evolution function can be derived with a variational scheme by minimizing the energy functional Eq. (9). The detailed derivative is shown in the Supporting Document of this paper. The evolution equation is

$$\frac{\partial\phi}{\partial t}=\delta[\phi(s)]\{-2[\alpha+(\beta*\mathbf{x})]+\ln P(y|-1)-\ln P(y|1)\}. \tag{11}$$

4 Integrating the MRF Model with Other AC Models

In this section, we incorporate the MRF functional in Eq. (9) with more standard AC functionals. We propose a specific implementation of the combined model.

4.1 *Combining Energy Functionals*

Equation (9) demonstrates how an MRF can be represented as an AC functional. However, since AC functionals are linear, the MRF functional can easily be combined with other advantageous functionals. In this direction, we incorporate regularization and edge terms with the MRF energy functional.

To promote a smooth contour during the evolution, we regularize the zero level set ϕ by penalizing its weighted Euclidean length of the curve $\mathbf{C}$ as[20]

$$E_R=\exp\left\{\int_{\mathbf{C}} g[y(s)]\mathrm{d}s\right\}, \tag{12}$$

where $g[y(s)]$ is defined as color gradient-based edge-detection function

$$g[y(s)]=\frac{1}{1+m[y(s)]}. \tag{13}$$

Here $m[y(s)]$ is the local structure tensor-based color gradient.[20] If $g[y(s)]$ is a constant, then Eq. (12) devolves into the boundary length. With the fact that $\|\nabla H(\phi)\|=\delta\{\phi[\mathbf{y}(c)]\}\|\nabla\phi\|$,[27] by applying Green's theorem to transform a line integral into an area integral in Eq. (12) and employing the Heaviside function $H(\phi)$, E_R reduces to

$$E_R(\phi)=\exp\left\{\int_S g[y(s)][\phi(s)]\|\nabla\phi\|\mathrm{d}s\right\}. \tag{14}$$

4.2 *Specific Implementation*

Assume $P[y(s)|x(s)]$ be multivariate Gaussian distribution

$$P[y(s)|x(s)]=\frac{1}{(2\pi)^{0.5k}|\Sigma|^{0.5}}\exp\{-0.5[y(s)-\mu]^T\Sigma[y(s)-\mu]\}. \tag{15}$$

This leads to the following evolution equation:

$$\begin{aligned}\frac{\partial\phi}{\partial t}&=\delta(\phi)\Big\{-2[\alpha+(\beta*\mathbf{x})]+[[\mathbf{y}(s)-\mu_2]^T\Sigma_2^{-1}[\mathbf{y}(s)-\mu_2] \\ &\quad -[y(s)-\mu_1]^T\Sigma_1^{-1}[y(s)-\mu_1]]+\log\frac{|\Sigma_2|}{|\Sigma_1|} \\ &\quad +\gamma g[\mathbf{y}(s)]\delta(\phi)\mathrm{div}\left(\frac{\nabla\phi}{|\nabla\phi|}\right)\Big\},\end{aligned} \tag{16}$$

where

$$\begin{aligned}&\mu_i=\frac{1}{|S_i|}\int_{S_i}y(s)\mathrm{d}s \quad \text{and} \\ &\Sigma_i=\frac{1}{|S_i|}\int_{S_i}[y(s)-\mu_i][y(s)-\mu_i]^T\mathrm{d}s, \quad (i\in\{1,2\}).\end{aligned} \tag{17}$$

4.3 *Model Parameters*

The convolution function β in Eq. (16) is determined as a kernel function

$$\beta=\frac{2\beta_0}{\pi}\arctan[0.2(t-1)]\times K(\cdot), \tag{18}$$

where t is the time in iterations and $K(\cdot)$ can be defined as Square kernel

$$\beta=\mathrm{SK}(x,\sigma), \tag{19}$$

where $\mathrm{SK}(x,\sigma)$ is an $(2\sigma+1)\times(2\sigma+1)$ square window centered at x, or the Gaussian kernel (GK)

$$\mathrm{GK}(x,\sigma)=\frac{1}{\sqrt{2\pi}}\exp\left(-\frac{x^2}{2\sigma^2}\right). \tag{20}$$

The other parameters in Eq. (16) are defined as $\alpha=\eta_c^2-1$, $\beta_0=0.001$, $\sigma=[(\eta_c-1)/2]$, and $\gamma=0.8$, where the η_c is a experientially defined 21×21 window centered at (excluding) pixel x.

Integrating the MRF functional into this result yields

$$E(\phi) = E_{\mathrm{MAP}}(\phi) + \gamma E_R(\phi),$$
$$= \int_S \Big\{ H(\phi)[2\alpha + (\beta * x) + \ln P(y|1) - \ln P(y|-1)] - \frac{1}{2}(\beta * x) - \alpha + \ln P(y|-1) \Big\} \mathrm{d}s + \gamma \int_S g[y(s)]\delta[\phi(s)]\|\nabla\phi\| \mathrm{d}s. \quad (21)$$

4.4 *Evolution Equation*

The curve evolution can be derived with variational scheme by minimizing the energy functional Eq. (21). The detailed derivative is shown in the Appendix. The evolution equation is

$$\frac{\partial\phi}{\partial t} = \delta[\phi(s)]\Big\{ -2[\alpha + (\beta * \mathbf{x})] + \ln P(\mathbf{y}|-1) - \ln P(\mathbf{y}|1) + \gamma g[\mathbf{y}(s)]\delta(\phi)\mathrm{div}\left(\frac{\nabla\phi}{|\nabla\phi|}\right)\Big\}. \quad (22)$$

5 Explicit Shape Descriptors for Gland Classification

Figure 1 shows the flowchart for automated gland segmentation using the MaRACel model and then ESDs to distinguish prostate glands of G3 and G4. The original image segmented by MaRACel as described in previous section. Using the segmentation results, ESDs[37] are employed to extract morphologic features. Finally, a trained SVM is used for classifying glands into G3 and G4.

6 Experimental Design

6.1 *Datasets*

6.1.1 *Dataset 1 (D1)*

- Data: 216 images were obtained from H&E-stained prostate core needle biopsy images digitized at 20× optical magnification using an Aperio whole-slide digital scanner. Each image includes one or more prostate gland.
- Ground truth generation: For all 216 images, the objective was to segment the gland boundaries. As it was impossible to have an expert pathologist manually segment every gland in each image (to provide ground truth for quantitative evaluation), the expert randomly picked regions (ROIs) of interest on the digitized images where clusters of glands were visible. The expert then meticulously segmented gland boundaries from within the randomly chosen ROIs. Consequently, quantitative evaluation of the different AC models was limited to these ROIs across the 216 images.

6.1.2 *Dataset 2 (D2)*

- Data: 352 regions which include at least one gland in each region were manually selected from 55 whole-slide prostate core needle biopsy images obtained from 11 patient studies from the Institute of Pathology at Case Western Reserve University. The tissue biopsy cores are stained with H&E and digitized using a high-resolution whole slide scanner Aperio ScanScope digitizer at 40× optical magnification.
- Ground truth generation: An expert pathologist was asked to manually outline the tumor regions into two subgroups: G3 and G4 on the digitized slides. One hundred and sixty one gland regions with G3 and 191 gland regions with G4 were selected from annotated tumor regions. Every gland contained within each region was segmented by an expert to obtain gland boundaries.
- Training and testing samples: We randomly chose 250 samples (112 G3 and 138 G4) as training samples and the remaining 102 samples (59 G3 and 57 G4) as testing samples. The classification on G3 and G4 glands only conducts on this data set.

6.2 *Comparative Strategies*

The four AC models that we implemented are (1) CV's model[27] with random initialization, (2) RD's model[30] with random initialization, (3) MaRACel with GK, and (4) MaRACel with

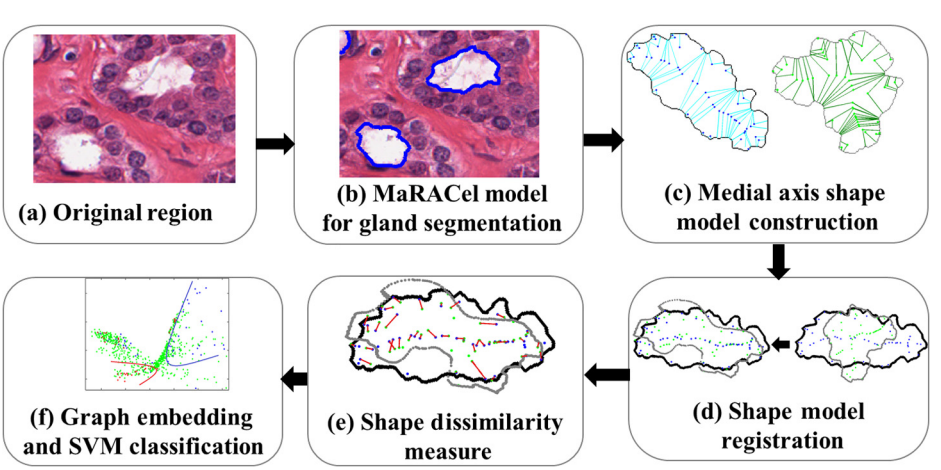

Fig. 1 The flowchart of automated gland segmentation with MaRACel model and ESDs for Gleason grading.

square kernel, for the purpose of (1) showing the performance of MaRACel with different kernels and (2) quantitatively comparing MaRACel with two popular region-based models.

6.3 *Experimental Evaluation*

Four AC models (CV, RD, MaRACel + GK, and MaRACel + SK) were evaluated in terms of their gland segmentation accuracy. The four models were randomly initialized with circles evenly distributed across the image. The models were evaluated based on region-based measurements as described in Sec. 6.4.1.

6.3.1 *Experiment 1: Comparison of MaRACel + GK against CV and RD models*

The aim of this experiment was to show the efficiency and accuracy of MaRACel + GK over the CV and RD models. Each model is used for gland segmentation on D1. Models were evaluated in terms of their gland segmentation accuracy.

6.3.2 *Experiment 2: Comparison of MaRACel + GK against MaRACel + SK*

The aim of this experiment was to compare the accuracy of MaRACel with two kernel types (Gaussian and square).

6.3.3 *Experiment 3: Automated classification of G3 and G4 glands on prostate histopathology*

The aim of this experiment is to show the effectiveness of automated segmentation results with the MaRACel model in distinguishing G3 and G4 glands.

6.4 *Performance Measures*

6.4.1 *Region-based overlapping measurements*

The performance of each model is evaluated based on the following region-based overlapping measurements. Gland segmentation results of the MaRACel and compared models were evaluated in terms of measures: Dice coefficient (DICE), overlap ratio (OL), sensitivity (SN), specificity (SP), and positive predictive value (PPV). For each image, the set of pixels lying within the manual delineations of the glands is denoted as $\mathcal{A}(G)$. The set of pixels lying within any boundary from a segmentation model are denoted as $\mathcal{A}(S)$. $\mathcal{A}(S)$ is comprised of those pixels whose level set functions are positive after convergence of AC models. $|\cdot|$ represents the number of pixels in a region, such that $|C|$ represents the total number of pixels in the image $\mathcal{C}$. DICE, OL, SN, SP, and PPV are then defined as

1. $\text{DICE} = \frac{2\times|\mathcal{A}(S)\cap\mathcal{A}(G)|}{|\mathcal{A}(S)|+|\mathcal{A}(G)|}$;
2. $\text{OL} = \frac{|\mathcal{A}(S)\cap\mathcal{A}(G)|}{|\mathcal{A}(S)\cup\mathcal{A}(G)|}$;
3. $\text{SN} = \frac{|\mathcal{A}(S)\cap\mathcal{A}(G)|}{|\mathcal{A}(G)|}$;
4. $\text{SP} = \frac{|\mathcal{C}-\mathcal{A}(S)\cap\mathcal{A}(G)|}{|\mathcal{C}-\mathcal{A}(G)|}$;
5. $\text{PPV} = \frac{|\mathcal{A}(S)\cap\mathcal{A}(G)|}{|\mathcal{A}(S)|}$.

The values shown in the table are the average values across 10 images. A Dice = OL = SN = SP = PPV = 1 is reflective of perfect segmentation.

6.4.2 *Classification performance in discriminating Gleason 3 and Gleason 4 glands*

Precision–recall curves [see Fig. 2(a)] and receiver operating characteristic (ROC) curves [see Fig. 2(b)] are used to assess the performance of classification of G3 and G4 glands segmented by different models. In Eq. (23), area under the ROC curve (AUC) involves computing the value of $p(r)$ over the interval between $r = 0$ and $r = 1$ where true-positive rate $p(r)$ is a function of false-positive rate r. The AUC is defined as

$$\text{AUC} = \int_0^1 p(r)\mathrm{d}r. \tag{23}$$

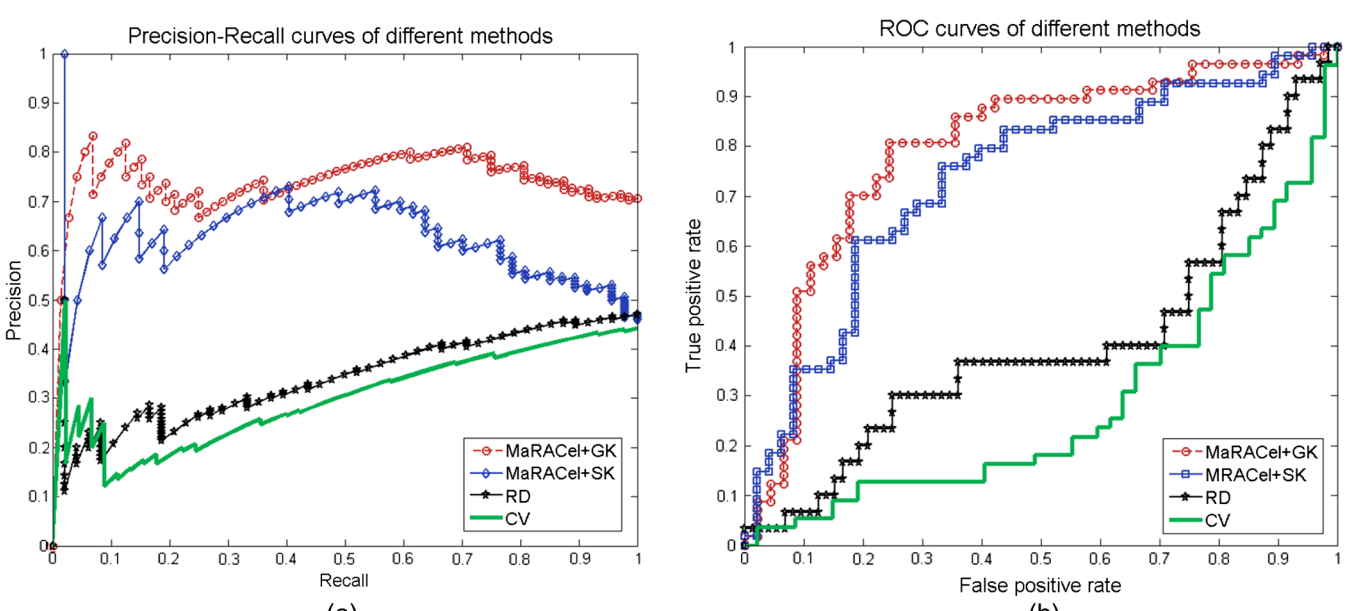

Fig. 2 (a) The precision–recall curves and (b) ROC curves for accuracy distinguishing G3 from G4 in D2 from four segmentation models.

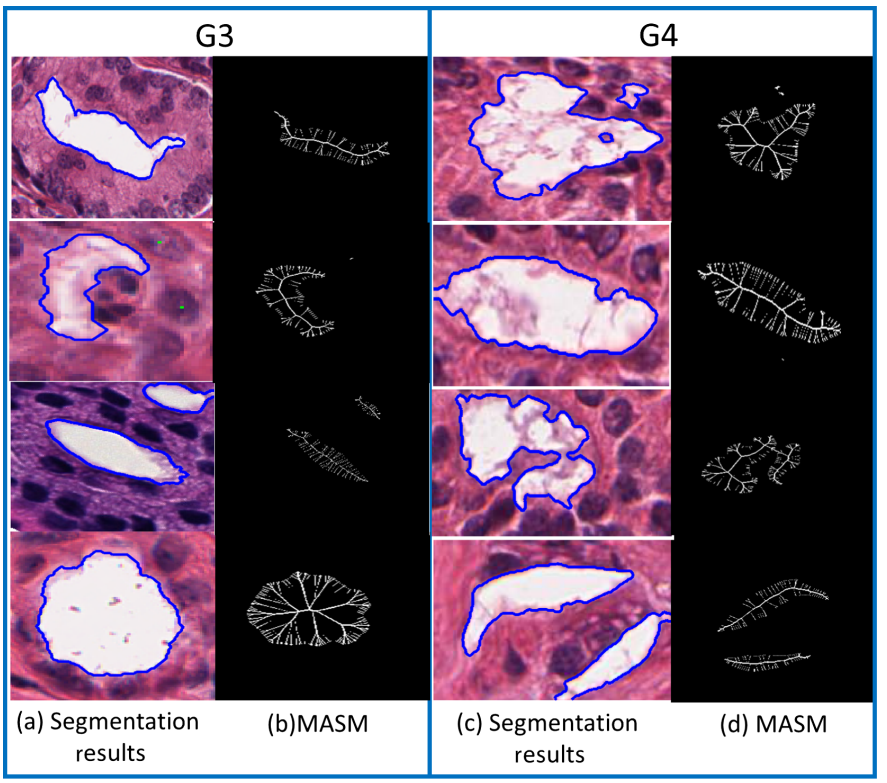

Fig. 3 (a and c) Example of automated segmentation results by MaRACel model and (b and d) visualization of medical axis shape model (MASM) for (a, b) G3 and (c, d) G4.

7 Results and Discussion

7.1 *Qualitative Results*

Example of automated segmentation results by MaRACel model and visualization of medical axis shape model (MASM) for G3 and G4 glands are shown in Fig. 3, respectively. The segmentation for the RD and CV models, shown in columns (b) and (c) in Fig. 4, reveals the inability of these models to eliminate the small, spurious regions that appear due to noise. That is, the CV and RD models inappropriately segment background regions within the glands. The segmentation results for MaRACel + SK and MaRACel + GK are given in column (d) and (e), respectively. MaRACel + SK and MaRACel + GK remove these false regions, yielding a single segmented region for each gland.

7.2 *Quantitative Results*

The quantitative evaluation of segmentation results CV, RD, MaRACel + SK, and MaRACel + GK models on two datasets is reported in Table 1. The results reflect improved performance of MaRACel + SK and MaRACel + GK models over CV and RD models. Figure 2 shows the precision–recall and ROC curves corresponding to gland classification with respect to the four models. MaRACel + SK and MaRACel + GK improved AUC compared to CV and RD models. Our MaRACel model, while superior to the state-of-the-art comparison models, has a lower AUC compared to manual gland segmentation in Ref. 37. This suggests that we have room for improvement in our automated segmentation approach.

This study represents a new model for gland segmentation and classification. The potential contribution of this work is that the work can be used for computational Gleason grading. The clinical performance of the model may require additional and extensive validation of the ability to predict patient outcomes under a variety of management choices, e.g., surgical

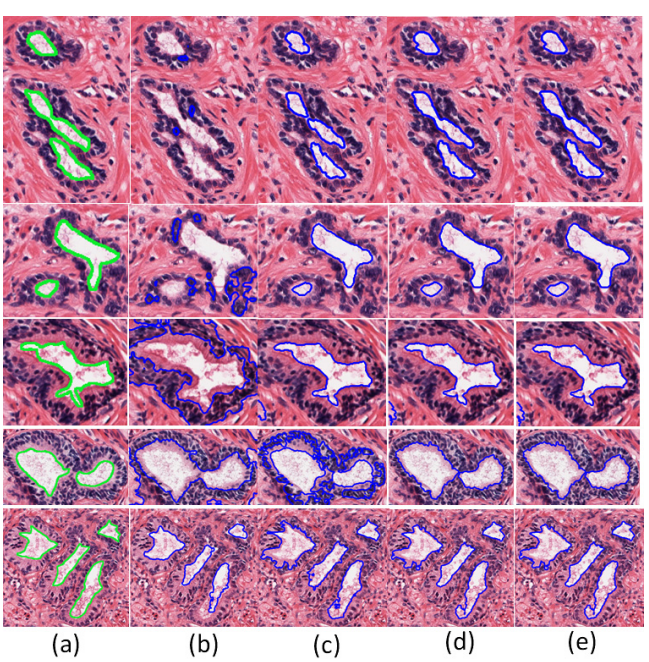

Fig. 4 Qualitative segmentation results with different methods. Different images are displayed from top to down. From left to right are (a) the ground truth (in green contours), (b) CV, (c) RD, (d) MaRACel + SK, and (e) MaRACel + GK (in blue contours).

Table 1 Quantitative evaluation of segmentation and classification results on D1 and D2 with CV, RD, MaRACel + SK, and MaRACel + GK models.

		Measurement					
		Segmentation measurement					Classification measurement
Models	Datasets	DICE (%)	OL (%)	SN (%)	SP (%)	PPV (%)	AUC
	D1	68.70 ± 12.88	61.62 ± 11.86	73.96 ± 11.34	80.66 ± 11.38	69.49 ± 14.72	
CV	D2	65.34 ± 10.39	55.69 ± 9.23	71.13 ± 11.42	75.69 ± 10.32	66.91 ± 12.33	0.28
	D1	81.54 ± 5.00	73.13 ± 5.41	83.22 ± 3.95	92.58 ± 3.97	84.79 ± 6.42	
RD	D2	66.72 ± 6.01	54.63 ± 6.39	80.72 ± 5.60	79.16 ± 7.20	69.14 ± 9.44	0.41
	D1	86.25 ± 4.25	79.49 ± 4.23	86.41 ± 3.20	94.26 ± 3.47	87.99 ± 4.97	
MaRACel + SK	D2	75.81 ± 3.40	63.98 ± 4.07	77.75 ± 5.26	78.49 ± 4.96	82.18 ± 3.89	0.73
	D1	86.25 ± 4.08	79.34 ± 4.11	86.80 ± 3.41	94.05 ± 3.70	87.60 ± 4.79	
MaRACel + GK	D2	76.59 ± 2.81	64.57 ± 3.35	80.91 ± 3.85	85.21 ± 3.01	78.15 ± 4.17	**0.80**

therapy, radiation therapy, and active surveillance. The MaRACel model does though have at least two limitations. One limitation is that it only focused on lumen region segmentation. The model has not been leveraged to detect or segment epithelium regions yet. Therefore, the epithelium/lumen ratios cannot be computed with this model. Also, the model was only tested on image tiles, instead of whole slide images. We will address these two issues in our future work. Also, we intend to integrate MaRACel with more efficient gland detection approaches.[20,45]

8 Concluding Remarks

In this paper, an MaRACel is presented for histological image segmentation. The formulation of the Markov prior is consistent with the continuous variational framework characteristic of ACs. The performance MaRACel is compared with the popular RAC models proposed by CV and RD with respect to the segmentation of prostatic acini (glands) and the differentiation of G3 and G4. MaRACel yielded higher average DICE, OLs, sensitivities, specificities, and PPVs both in terms of segmentation accuracy and ability to discriminate between G3 and G4 than CV and RD models.

Appendix

A.1 Derivation of Curve Evolution Function with the Theory of Calculus of Variations

Let us rewrite the energy functional Eq. (21) in the main body as

$$E(\phi)=\int_S\Big\{H(\phi)[2\alpha+(\beta*\mathbf{x})+\ln P(y|1)-\ln P(y|-1)] -\frac{1}{2}(\beta*\mathbf{x})-\alpha+\ln P(y|-1)+\gamma g[\mathbf{y}(s)]\delta[\phi(s)]\|\nabla\phi\|\Big\}\mathrm{d}s =\int_S F(\phi,s)\mathrm{d}s, \tag{24}$$

where

$$\boldsymbol{F}(\phi,s)=H(\phi)[2\alpha+(\beta*\mathbf{x})+\ln P(y|1)-\ln P(y|-1)] -\frac{1}{2}(\beta*\mathbf{x})-\alpha+\ln P(y|-1)+\gamma g[\mathbf{y}(s)]\delta[\phi(s)]\|\nabla\phi\|.$$

Based on the theory of calculus of variations, the energy function $E(\phi)$ will be minimized when the following Euler–Lagrange differential equation of the energy functional is satisfied

$$\frac{\partial\phi}{\partial t}=-\left\{\frac{\partial F}{\partial\phi}-\frac{\partial}{\partial\xi}\frac{\partial F}{\partial\phi_\xi}-\frac{\partial}{\partial\zeta}\frac{\partial F}{\partial\phi_\zeta}\right\}. \tag{25}$$

First, we compute the first term $\partial F/\partial\phi$ on the right-hand side of Eq. (25).

The introduction of the convolution equation $\beta*\mathbf{x}$ into the AC energy function is new to this paper, and consequently, the formation of its functional derivative may be unfamiliar. Accordingly, we now provide a derivation. Consider first the individual functional derivatives of the two terms in Eq. (9) of the main body containing the convolution equation

$$\frac{\partial}{\partial\phi}\left[\frac{1}{2}(\beta*\mathbf{x})\right]=\frac{\partial}{\partial\phi}\left[\frac{1}{2}\int_S\{2H[\phi(r)]-1\}\beta(s-r)\mathrm{d}r\right] =\frac{\partial}{\partial\phi}\int_S H[\phi(r)]\beta(s-r)\mathrm{d}r-\frac{1}{2}\frac{\partial}{\partial\phi}\int_S\beta(s-r)\mathrm{d}r =\delta[\phi(s)]\int_S\beta(s-r)\mathrm{d}r \tag{26}$$

and

$$\begin{aligned}
&\frac{\partial}{\partial\phi}\{H[\phi(s)](\beta * \mathbf{x})\} \\
&= \frac{\partial}{\partial\phi}\left\{H[\phi(s)]\left[\int_S \{2H[\phi(r)]-1\}\beta(s-r)\mathrm{d}r\right]\right\} \\
&= \frac{\partial}{\partial\phi}\int_S 2H[\phi(s)]H[\phi(r)]\beta(s-r)\mathrm{d}r \\
&\quad - \frac{\partial}{\partial\phi}\int_S H[\phi(s)]\beta(s-r)\mathrm{d}r \\
&= \delta[\phi(s)]\int_S 4H[\phi(r)]\beta(s-r)\mathrm{d}r - \delta[\phi(s)]\int_S \beta(s-r)\mathrm{d}r.
\end{aligned} \tag{27}$$

The first term in Eq. (25) results from a derivation very similar to that used for the Coulomb potential energy functional.[46] Finally, the functional derivative of the first term on the right-hand side of Eq. (25) is

$$\begin{aligned}
\frac{\partial F}{\partial\phi} &= \frac{\partial}{\partial\phi}\left\{H[\phi(s)][(\beta * x)(s) + 2\alpha + \ln P(y|1)\right. \\
&\quad \left. - \ln P(y|-1)] - \frac{1}{2}(\beta * x)(s) + \gamma g[\mathbf{y}(s)]\delta[\phi(s)]\|\nabla\phi\|\right\} \\
&= \delta[\phi(s)]\left(\int_S \{4H[\phi(r)]-2\}\beta(s-r)\mathrm{d}r + 2\alpha + \ln P(y|1)\right. \\
&\quad \left. - \ln P(y|-1)\right) + \gamma g[\mathbf{y}(s)]\|\nabla\phi\| \cdot \frac{\mathrm{d}\delta[\phi(s)]}{\mathrm{d}\phi} \\
&= 2\delta[\phi(s)](\beta * \mathbf{x})(s) - 2\delta[\phi(s)]\int_S \beta(s-r)\mathrm{d}r + 2\alpha \\
&\quad + \ln P(y|1) - \ln P(y|-1) + \gamma g[\mathbf{y}(s)]\|\nabla\phi\| \cdot \frac{\mathrm{d}\delta(\phi(s)}{\mathrm{d}\phi}.
\end{aligned} \tag{28}$$

The second and the third terms on the right-hand side of Eq. (25) can be computed as

$$\begin{aligned}
\frac{\partial}{\partial\xi}\frac{\partial F}{\partial\phi_\xi} + \frac{\partial}{\partial\zeta}\frac{\partial F}{\partial\phi_\zeta} &= \frac{\partial}{\partial\xi}\left\{\gamma g[\mathbf{y}(s)]\delta(\phi)\frac{\partial\|\nabla\phi\|}{\partial\phi_\xi}\right\} \\
&\quad + \frac{\partial}{\partial\zeta}\left\{\gamma g[\mathbf{y}(s)]\delta(\phi)\frac{\partial\|\nabla\phi\|}{\partial\phi_\zeta}\right\}.
\end{aligned} \tag{29}$$

As $\|\nabla\phi\| = \sqrt{\phi_\xi^2 + \phi_\zeta^2}$, taking derivative with respective to ϕ_ξ and ϕ_ζ, respectively, on both side of the equation yields

$$\frac{\partial\|\nabla\phi\|}{\partial\phi_\xi} = \frac{\phi_\xi}{\|\nabla\phi\|}, \tag{30}$$

$$\frac{\partial\|\nabla\phi\|}{\partial\phi_\zeta} = \frac{\phi_\zeta}{\|\nabla\phi\|}. \tag{31}$$

By substituting Eqs. (30) and (31) into Eq. (29), we can get

$$\begin{aligned}
\frac{\partial}{\partial\xi}\frac{\partial F}{\partial\phi_\xi} + \frac{\partial}{\partial\zeta}\frac{\partial F}{\partial\phi_\zeta} &= \frac{\partial}{\partial\xi}\left\{\gamma g[\mathbf{y}(s)]\delta(\phi)\frac{\phi_\xi}{\|\nabla\phi\|}\right\} \\
&\quad + \frac{\partial}{\partial\zeta}\left\{\gamma g[\mathbf{y}(s)]\delta(\phi)\frac{\phi_\zeta}{\|\nabla\phi\|}\right\} \\
&= \gamma g[\mathbf{y}(s)]\mathrm{div}\left[\delta(\phi)\frac{\nabla\phi}{\|\nabla\phi\|}\right].
\end{aligned} \tag{32}$$

Here, we have used the facts

$$\begin{aligned}
&\mathrm{div}\left(\left\{\gamma g[\mathbf{y}(s)]\gamma(\phi)\frac{\phi_\xi}{\|\nabla\phi\|}\right\}, \left\{\beta g[\mathbf{y}(s)]\delta(\phi)\frac{\phi_\zeta}{\|\nabla\phi\|}\right\}\right) \\
&= \frac{\partial}{\partial\xi}\left\{\beta g[\mathbf{y}(s)]\delta(\phi)\frac{\phi_\xi}{\|\nabla\phi\|}\right\} + \frac{\partial}{\partial\zeta}\left\{\beta g[\mathbf{y}(s)]\delta(\phi)\frac{\phi_\zeta}{\|\nabla\phi\|}\right\},
\end{aligned} \tag{33}$$

and

$$\nabla\phi = (\phi_\xi, \phi_\zeta)^T. \tag{34}$$

In Eq. (32), $\mathrm{div}[\delta(\phi)(\nabla\phi/|\nabla\phi|)]$ can be computed as

$$\mathrm{div}\left[\delta(\phi)\frac{\nabla\phi}{\|\nabla\phi\|}\right] = \delta(\phi)\mathrm{div}\left(\frac{\nabla\phi}{\|\nabla\phi\|}\right) + \nabla\delta(\phi)\frac{\nabla\phi}{\|\nabla\phi\|}. \tag{35}$$

From the second term on the right-hand side of Eq. (35), we have

$$\nabla\delta(\phi)\frac{\nabla\phi}{\|\nabla\phi\|} = \frac{d\delta(\phi)}{d\phi}\cdot(\phi_\xi^2 + \phi_\zeta^2)\cdot\frac{1}{\|\nabla\phi\|} = \frac{d\delta(\phi)}{d\phi}\cdot\|\nabla\phi\| \tag{36}$$

With Eqs. (32), (35), and (36),

$$\begin{aligned}
\frac{\partial}{\partial\xi}\frac{\partial F}{\partial\phi_\xi} + \frac{\partial}{\partial\zeta}\frac{\partial F}{\partial\phi_\zeta} &= \gamma g[\mathbf{y}(s)]\delta(\phi)\mathrm{div}\left(\frac{\nabla\phi}{\|\nabla\phi\|}\right) \\
&\quad + \gamma g[\mathbf{y}(s)]\frac{d\delta(\phi)}{d\phi}\|\nabla\phi\|
\end{aligned} \tag{37}$$

Substituting Eqs. (28) and (37) into Eq. (25), we finally get the curve evolution function as

$$\begin{aligned}
\frac{\partial\phi}{\partial t} &= \delta[\phi(s)]\left\{-2[\alpha + (\beta * \mathbf{x})] + \ln P(y|-1)\right. \\
&\quad \left. - \ln P(y|1) + \gamma g[\mathbf{y}(s)]\delta(\phi)\mathrm{div}\left(\frac{\nabla\phi}{\|\nabla\phi\|}\right)\right\}.
\end{aligned} \tag{38}$$

Disclosures

No conflicts of interest, financial or otherwise, are declared by the authors.

Acknowledgments

Research reported in this publication was supported by the National Natural Science Foundation of China (No. 61273259); Six Major Talents Summit of Jiangsu Province (No. 2013-XXRJ-019), and the Natural Science Foundation of Jiangsu Province of China (No. BK20141482) and Jiangsu Innovation

and Entrepreneurship Group Talents Plan (No. JS201526); the National Cancer Institute of the National Institutes of Health under award numbers 1U24CA199374-01, R01CA202752-01A1, R21CA179327-01, and R21CA195152-01, the National Institute of Diabetes and Digestive and Kidney Diseases under award number R01DK098503-02, the National Center for Research Resources under award number 1 C06 RR12463-01, the DOD Prostate Cancer Synergistic Idea Development Award (PC120857), the DOD Lung Cancer Idea Development New Investigator Award (LC130463), the DOD Prostate Cancer Idea Development Award, the Case Comprehensive Cancer Center Pilot Grant, VelaSano Grant from the Cleveland Clinic, the Wallace H. Coulter Foundation Program in the Department of Biomedical Engineering at Case Western Reserve University. The content is solely the responsibility of the authors and does not necessarily represent the official views of the National Institutes of Health.

References

1. S. Geman and D. Geman, "Stochastic relaxation, Gibbs distribution, and the Bayesian restoration of images," *IEEE Trans. Pattern Anal. Mach. Intell.* **PAMI-6**, 721–741 (1984).
2. M. Kass, A. Witkin, and D. Terzopoulos, "Snakes: active contour models," *Int. J. Comput. Vision* **1**(4), 321–331 (1988).
3. T. N. Pappas, "An adaptive clustering algorithm for image segmentation," *IEEE Trans. Signal Process.* **40**, 901–914 (1992).
4. C. A. Bouman and M. Shapiro, "A multiscale random field model for Bayesian image segmentation," *IEEE Trans. Image Process.* **3**, 162–177 (1994).
5. J. Wu and A. C. S. Chung, "A segmentation model using compound Markov random fields based on a boundary model," *IEEE Trans. Image Process.* **16**, 241–252 (2007).
6. G. McGarry and M. Deriche, "Mammographic image segmentation using a tissue-mixture model and Markov random fields," in *Proc. Int. Conf. on Image Processing*, Vol. 3, pp. 416–419 (2000).
7. A. Farag, A. El-Baz, and G. Gimel'farb, "Precise segmentation of multimodal images," *IEEE Trans. Image Process.* **15**, 952–968 (2006).
8. S. P. Awate and R. T. Whitaker, "Feature-preserving MRI denoising: a nonparametric empirical Bayes approach," *IEEE Trans. Med. Imaging* **26**, 1242–1255 (2007).
9. X. Liu et al., "Prostate cancer segmentation with simultaneous estimation of Markov random field parameters and class," *IEEE Trans. Med. Imaging* **28**, 906–915 (2009).
10. B. Scherrer et al., "Distributed local MRF models for tissue and structure brain segmentation," *IEEE Trans. Med. Imaging* **28**, 1278–1295 (2009).
11. Z. Kato and T. Pong, "A Markov random field image segmentation model for color textured images," *Image Vision Comput.* **24**(10), 1103–1114 (2006).
12. F. Leymarie and M. Levine, "Tracking deformable objects in the plane using an active contour," *IEEE Trans. Pattern Anal. Mach. Intell.* **15**(6), 617–634 (1993).
13. V. Chalana et al., "A multiple active contour model for cardiac boundary detection on echocardiographic sequences," *IEEE Trans. Med. Imaging* **15**(3), 290–298 (1996).
14. I. Mikic, S. Krucinski, and J. Thomas, "Segmentation and tracking in echocardiographic sequences: active contours guided by optical flow estimates," *IEEE Trans. Med. Imaging* **17**(2), 274–284 (1998).
15. A. Tsai et al., "A shape-based approach to the segmentation of medical imagery using level sets," *IEEE Trans. Med. Imaging* **22**(2), 137–154 (2003).
16. C. Pluempitiwiriyawej et al., "STACS: new active contour scheme for cardiac MR image segmentation," *IEEE Trans. Med. Imaging* **24**(5), 593–603 (2005).
17. W. Fang et al., "Incorporating temporal information into level set functional for robust ventricular boundary detection from echocardiographic image sequence," *IEEE Trans. Biomed. Eng.* **55**(11), 2548–2556 (2008).
18. I. Ben Ayed, S. Li, and I. Ross, "Embedding overlap priors in variational left ventricle tracking," *IEEE Trans. Med. Imaging* **28**(12), 1902–1913 (2009).
19. B. Al-Diri, A. Hunter, and D. Steel, "An active contour model for segmenting and measuring retinal vessels," *IEEE Trans. Med. Imaging* **28**(9), 1488–1497 (2009).
20. J. Xu et al., "A high-throughput active contour scheme for segmentation of histopathological imagery," *Med. Image Anal.* **15**, 851–862 (2011).
21. H. Fatakdawala et al., "Expectation-maximization-driven geodesic active contour with overlap resolution (EMaGACOR): application to lymphocyte segmentation on breast cancer histopathology," *IEEE Trans. Biomed. Eng.* **57**, 1676–1689 (2010).
22. J. Xu, J. P. Monaco, and A. Madabhushi, "Markov random field driven region-based active contour model (MaRACel): application to medical image segmentation," *Lect. Notes Comput. Sci.* **6363**, 197–204 (2010).
23. M. Rochery, I. Jermyn, and J. Zerubia, "Higher order active contours," *Int. J. Comput. Vision* **69**, 27–42 (2006).
24. P. Horváth et al., "A higher-order active contour model of a 'gas of circles' and its application to tree crown extraction," *Pattern Recognit.* **42**, 699–709 (2009).
25. T. Peng et al., "Extended phase field higher-order active contour models for networks," *Int. J. Comput. Vision* **88**, 111–128 (2010).
26. D. Mumford and J. Shah, "Optimal approximations by piecewise smooth functions and associated variational problems," *Commun. Pure Appl. Math.* **42**(5), 577–685 (1989).
27. T. F. Chan and L. A. Vese, "Active contours without edges," *IEEE Trans. Image Process.* **10**(2), 266–277 (2001).
28. X. Yang et al., "An efficient MRF embedded level set method for image segmentation," *IEEE Trans. Image Process.* **24**, 9–21 (2015).
29. Z. Shahvaran et al., "Variational level set combined with Markov random field modeling for simultaneous intensity non-uniformity correction and segmentation of MR images," *J. Neurosci. Methods* **209**(2), 280–289 (2012).
30. D. Cremers, M. Rousson, and R. Deriche, "A review of statistical approaches to level set segmentation: integrating color, texture, motion and shape," *Int. J. Comput. Vision* **72**, 195–215 (2007).
31. A. W. Partin et al., "Morphometric measurement of tumor volume and per cent of gland involvement as predictors of pathological stage in clinical stage B prostate cancer," *J. Urol.* **141**(2), 341–345 (1989).
32. S. Naik et al., "Gland segmentation and computerized Gleason grading of prostate histology by integrating low-, high-level and domain specific information," in *MIAAB Workshop*, pp. 1–8, Citeseer (2007).
33. K. Nguyen, A. Sarkar, and A. K. Jain, "Prostate cancer grading: use of graph cut and spatial arrangement of nuclei," *IEEE Trans. Med. Imaging* **33**, 2254–2270 (2014).
34. K. Nguyen, B. Sabata, and A. K. Jain, "Prostate cancer grading: gland segmentation and structural features," *Pattern Recognit. Lett.* **33**(7), 951–961 (2012).
35. K. Sirinukunwattana, D. R. J. Snead, and N. M. Rajpoot, "A stochastic polygons model for glandular structures in colon histology images," *IEEE Trans. Med. Imaging* **34**, 2366–2378 (2015).
36. C. Gunduz-Demir et al., "Automatic segmentation of colon glands using object-graphs," *Med. Image Anal.* **14**(1), 1–12 (2010).
37. R. Sparks and A. Madabhushi, "Explicit shape descriptors: novel morphologic features for histopathology classification," *Med. Image Anal.* **17**(8), 997–1009 (2013).
38. R. Sparks and A. Madabhushi, "Statistical shape model for manifold regularization: Gleason grading of prostate histology," *Comput. Vision Image Understanding* **117**, 1138–1146 (2013).
39. J. Besag, "Spatial interaction and the statistical analysis of lattice systems," *J. R. Stat. Soc. Ser. B (Methodol.)* **36**(2), 192–236 (1974).
40. D. Geman, "Random fields and inverse problems in imaging," in *Lecture Notes in Mathematics*, Vol. **1427**, pp. 113–193, Springer-Verlag (1991).
41. E. Ising, "Beitrag zur theorie des ferromagnetismus," *Z. Phys.* **31**, 253–258 (1925).
42. R. Duda, P. Hart, and D. Stork, *Pattern Classification*, John Wiley & Sons (2001).
43. S. Osher and J. A. Sethian, "Fronts propagating with curvature-dependent speed: algorithms based on Hamilton-Jacobi formulations," *J. Comput. Phys.* **79**(1), 12–49 (1988).

44. S. C. Zhu and A. Yuille, "Region competition: unifying snakes, region growing, and Bayes/MDL for multiband image segmentation," *IEEE Trans. Pattern Anal. Mach. Intell.* **18**, 884–900 (1996).
45. K. Sirinukunwattana et al., "Gland segmentation in colon histology images: the GlaS challenge contest," *Med. Image Anal.* **35**, 489–502 (2017).
46. R. G. Parr and W. Yang, *Density-Functional Theory of Atoms and Molecules*, Vol. **16**, Oxford University Press (1989).

Jun Xu is a full professor at Nanjing University of Information Science and Technology, China. He received his MS degree in applied mathematics from the University of Electronic Science and Technology of China and his PhD in control science and engineering from Zhejiang University, China. His other academic experiences include work as post-doc associate and research assistant at Rutgers University and a visiting assistant professor at Case Western Reserve University. His research interests include medical image analysis and digital pathology.

James P. Monaco received his bachelor's degree in computer engineering and his master's degree in electrical engineering from Texas A&M University. He earned a PhD in electrical engineering from the University of Texas. His other academic experiences include work as a post-doc and assistant research professor at Rutgers University and a visiting scholar at the University of Michigan. He also has over 15 years of diverse industry experience. Currently, he is the lead scientist at Inspirata Inc., leading the company's research and development for its companion diagnostics systems.

Rachel Sparks received her PhD in biomedical engineering from Rutgers, the State University of New Jersey, USA, in 2014, where she developed algorithms for prostate cancer analysis and registration of prostate MRI and transrectal ultrasound. She is currently a post-doc research associate at the Centre for Medical Image Computing at the University College of London, United Kingdom, where she is developing algorithms for real-time surgical planning and guidance for the Epilepsy-Navigator (EpiNavTM) software platform.

Anant Madabhushi is the director of the Center for Computational Imaging and Personalized Diagnostics (CCIPD) and the F. Alex Nason professor II in the Departments of Biomedical Engineering, Pathology, Radiology, Radiation Oncology, Urology, General Medical Sciences, and Electrical Engineering and Computer Science at Case Western Reserve University. He is also a member of the Case Comprehensive Cancer Center. He has authored over 115 peer-reviewed journal publications and over 150 conferences papers and delivered over 175 invited talks and lectures both in the United States and abroad.